Interfacial La diffusion in CeO$_2$/LaFeO$_3$ hybrid for enhanced oxygen evolution activity

Yawen Dai[1], Jie Yu[1], Zhenbao Zhang[1], Chun Cheng[1], Peng Tan[2], Zongping Shao[3,*],

Meng Ni[1,*]

[1]Department of Building and Real Estate, The Hong Kong Polytechnic University, Hung Hom, Kowloon, Hong Kong, China.

[2]Department of Thermal Science and Energy Engineering, University of Science and Technology of China, Hefei 230026, Anhui, China.

[3]State Key Laboratory of Materials-Oriented Chemical Engineering, College of Chemical Engineering, Nanjing Tech University, No. 5 Xin Mofan Road, Nanjing 210009, P. R. China

[*]Corresponding authors

E-mail addresses: shaozp@njtech.edu.cn (Zongping Shao); meng.ni@polyu.edu.hk (Meng Ni)

Abstract

Electrochemical oxygen evolution reaction (OER) is of great significance for energy conversion and storage. The hybrid strategy is attracting increasing interests for the development of highly active OER electrocatalysts. Regarding the activity enhancement mechanism, the electron coupling between two phases in hybrids has been widely reported, but the interfacial elemental redistribution is rarely investigated. Herein, we developed a $CeO_2/LaFeO_3$ hybrid electrocatalyst for enhanced OER activity. Interestingly, a selective interfacial La diffusion from $LaFeO_3$ to CeO_2 was demonstrated by the electron energy loss spectra and elemental mapping. This redistribution of cations triggers the change of chemical environment of interface elements for charge compensation due to the electro-neutrality principle, which results in increased oxygen vacancies and high-valent Fe species that promote the OER electrocatalysis. This mechanism might be extended to other hybrid systems and inspire the design of more efficient electrocatalysts.

Keywords: oxygen evolution, interface engineering, elemental redistribution, perovskite oxide

Introduction

Oxygen evolution reaction (OER) is a pivotal electrochemical reaction for many clean-energy technologies, such as solar/electricity-driven water splitting, carbon dioxide reduction, and rechargeable metal-air batteries.[1-3] However, OER is a 4-electron involved reaction with sluggish kinetics and large overpotentials, which greatly limits the energy conversion efficiencies and practical applications of the above technologies.[4] Therefore, accelerating OER by efficient electrocatalysts is essential but still challenging.

Building hybrids is an efficient strategy in the electrocatalysis field, where the hybrids often display higher activity than their single-component counterparts.[5-7] It could combine the advantages of different materials and realize diverse synergistic effects to promote the OER.[8,9] Besides, the hybrids could also integrate specific active sites which are responsible for different sub-steps for the multi-step OER.[10,11] More importantly, the interaction between the two phases of a hybrid offers new opportunity

for electronic structure regulation, and thus it could enhance the intrinsic activity of active sites.[12,13] The interfacial electron coupling in various types of hybrid electrocatalysts has been reported, such as metal oxide/metal oxide,[14] metal oxide/metal,[12,15] and metal oxide (or metal)/carbon.[16,17] The interfacial electron transfer between two phases is suggested to play a key role in facilitating OER by tuning the local electron density,[7,18] creating defects,[14,19] or increasing the electron mobility.[20] In addition to the electron transfer, elemental redistribution between two phases is possible at the interface of hybrids. For example, Kim et al. reported a Mn diffusion in $La_{0.5}Mn_{0.5}O_3/Co_3O_4$ hybrid, which resulted in a new interlayer of $MnCo_2O_4$ that greatly promoted the OER and oxygen reduction activity.[21] However, as compared to interfacial electron transfer, the study about interfacial elemental redistribution is very limited for hybrid electrocatalysts.

The low-cost and nontoxic CeO_2 has been widely reported as an OER promoter in a lot of hybrid electrocatalyst systems.[22-24] Although CeO_2 alone is catalytically inactive, it has unique properties of flexible transition between Ce^{3+} and Ce^{4+} oxidation states and reversible oxygen ion exchange.[6,25] Hence, when constructing a hybrid between CeO_2 and a parent OER electrocatalyst, it could generate strong electron coupling and greatly assist the OER catalysis. Du et al reported a $CeO_2/Ni(OH)_2$ nanosheet hybrid, where the CeO_2 could accelerate the oxidation of Ni^{II} to $Ni^{II/IV}$, and thus lower the overpotential of OER.[25] Chai et al reported a CeO_2/Co_3O_4 nanotube hybrid. They demonstrated that the interfacial electron transfer could induce Co^{2+} octahedral sites and oxygen vacancies that benefited the OER process.[14] Liu et al. reported a CeO_2/Co_3O_4 nanosheet hybrid for OER, where they found remarkable 2D electron gas at the interface which renders outstanding electronic conductivity.[20] Despite the abundant study about the interfacial electron transfer of CeO_2-involved hybrid electrocatalysts, the interfacial elemental redistribution between CeO_2 and the OER parent catalyst has never been reported. Herein, we choose the $CeO_2/LaFeO_3$ hybrid as the model system. CeO_2 nanoparticles were deposited on $LaFeO_3$ by a facile chemical bath method, realizing enhanced OER activity. Interestingly, beside the general interfacial electron transfer between the two phases, we also

observed a selective interfacial La diffusion from LaFeO$_3$ to CeO$_2$. Furthermore, according to the electro-neutrality principle, this interfacial redistribution of positively charged cations could further facilitate the formation of oxygen vacancies and high-valent Fe species, and thus promoted the OER activity.

Experimental

Material synthesis

LaFeO$_3$ was synthesized by a conventional sol-gel method. 0.03 mol La(NO$_3$)$_3$·6H$_2$O and 0.03 mol Fe(NO$_3$)$_3$·9H$_2$O were dissolved in 20 mL H$_2$O. 0.06 mol ethylenediaminetetraacetic acid, 0.12 citric acid, and 48 mL NH$_3$·H$_2$O (25%) were dissolved in 15 mL H$_2$O, which was dropped into the metal nitrate solution to get a homogeneous mixture. The above mixture was heated under continuous stirring on a hot plate to form an orange transparent gel, followed by keeping the gel at 180 °C in oven for 12 h to get the black foamlike precursor. The precursor was heated in a furnace in air to 800 °C at 5 °C min^{-1} and then kept at 800 °C for 5 h to get the LaFeO$_3$ (LF) yellow powders.

CeO$_2$ nanoparticles were decorated on LF by a facile chemical bath process. 0.6x (x represents the molar ratio of Ce/Fe) mmol Ce(NO$_3$)$_3$·6H$_2$O were dissolved in 3 mL H$_2$O, followed by the addition of 0.6 mmol LF and a continuous stirring of 10 min. Then 2 mL NH$_3$·H$_2$O (25%) were dropwise added, and the mixture were stirred for another 10 min. The above mixture was then heated on the hot plate until the solvent was fully evaporated. The obtained solid were further heated in the oven at 200 °C for 4 h to fully decompose the NH$_4$NO$_3$ by-product and get the final product of hybrid LF-xCe (x=0.1, 0.25, 0.5). To prepare the LF-control sample, the pristine LF was treated with the same process described above in the mixed solution of HNO$_3$ (pH=3.8, the same with that of the Ce(NO$_3$)$_3$ solution when x=0.25) and NH$_3$·H$_2$O in the absence of Ce.

Characterization

The X-ray diffraction (XRD) patterns were collected by a powder X-ray diffractometer (Rigaku SmartLab 9kW-Advance) with Cu Kα irradiation source at a rate of 20° min^{-1}. The Raman spectra were recorded using a Renishaw Micro-Raman Spectroscopy System, with an excitation wavelength of 532 nm and intensity of 0.5 mW. A TESCAN VEGA3 field emission scanning electron microscope (SEM) were used to observe the micromorphology of samples. High resolution transmission electron microscopy (TEM) images and were acquired via a JEOL-Model-JEM-2100F field emission electron microscope at an accelerating voltage of 200 kV. Cs-corrected TEM images, energy dispersive X-ray spectroscopy (EDX), electron energy loss spectroscopy (EELS), and the elemental mapping were carried out on a JEOL JEM-ARM300F operating at 300kV. The specific surface areas were measured by the N_2 adsorption-desorption isotherms at 77.35 K and calculated using the Brunauer−Emmett−Teller (BET) method. The oxidation states of surface elements were identified through X-ray photoelectron spectroscopy (XPS) using a Nexsa XPS system. The spectra were fitted using the XPSPEAK41 software, and the different valent species were quantified by the peak area.

Electrochemical tests

5 mg as-prepared bare or hybrid electrocatalysts, 2.5 mg conductive carbon (Super P Li), 0.47 mL isopropanol, 0.1 mL H_2O, and 0.03 mL 5 wt% Nafion solution were mixed and sonicated to get a homogenous ink. 0.012 mL ink was dropped on a rotating disk electrode (RDE, 5 mm in diameter) to realize a catalyst loading of 0.5 mg cm^{-2}. All the electrochemical tests were carried out via a Solartron potentiostat using a three-electrode system, with the RDE as the working electrode, a graphite rod as the counter electrode, a Hg/HgO electrode as the reference electrode, and 0.1 M or 1 M KOH as the electrolyte. The OER activity was assessed by the linear sweep voltammetry (LSV) at a rate of 5 mV s^{-1}. The electrochemical impedance spectra (EIS) were recorded at 0.7 V vs. Hg/HgO with a perturbation amplitude of 10 mV. To enable the characterization of the electrocatalysts after long-term durability test, the electrocatalyst ink was dropped on a 1 cm * 1.5 cm carbon paper to realize a loading

mass of 2 mg cm^{-2}. After natural drying, the electrocatalyst-coated carbon paper was used as the working electrode to carry out the chronopotentiometry test.

Results and discussion

The XRD patterns of the bare and hybrid samples were displayed in Figure 1. A pure orthorhombic perovskite structure with a space group of *Pnma* (PDF#37-1493) was confirmed for the bare LF. With the increasing Ce loading on LF, the characteristic peak of CeO_2 can be identified for LF-0.5Ce, and no other impurity phase was observed. The sharp diffraction peaks of LF and the broad diffraction peaks of CeO_2 indicate the large and small crystal size, respectively. The coexistence of the two phases in the hybrids was further validated by Raman spectra (Figure S1). The $LaFeO_3$ (121) peak from 31° to 33° was zoomed in. As compared to the bare LF, the diffraction peaks of the LF phase in hybrids shift to larger angles, which indicates the lattice shrinkage. The lattice shrinkage might be due to the presence of high valent Fe^{4+} (0.585 Å) that has a smaller ionic radius than Fe^{3+} (0.645 Å), or the deficiency of lattice atoms.[26-28] Besides, the zoom-in image from 27° to 30° (CeO_2 (111) peak) shows that the diffraction peak of hybrid-CeO_2 shifts to a lower angle as compared to that of the bare CeO_2, indicating the lattice expansion. The hybrid-induced lattice distortion of LF and CeO_2 implies the strong interaction between the two phases, which enables the efficient regulation of electronic structure. The in-depth reason of the lattice distortion will be discussed more detailly latter combining other characterizations. The BET surface area (Figure S2) of LF-0.1Ce (6.78 m^2 g^{-1}) and LF-0.25Ce (6.76 m^2 g^{-1}) is slightly higher than that of the bare LF (4.97 m^2 g^{-1}), which can be attributed to the increased surface roughness caused by the nano-size CeO_2 decoration. When further increasing the Ce loading, the decreased specific surface area of LF-0.5Ce (3.72 m^2 g^{-1}) as compared to the bare LF is due to the particle aggregation, which agrees well with the SEM observation (Figure S3).
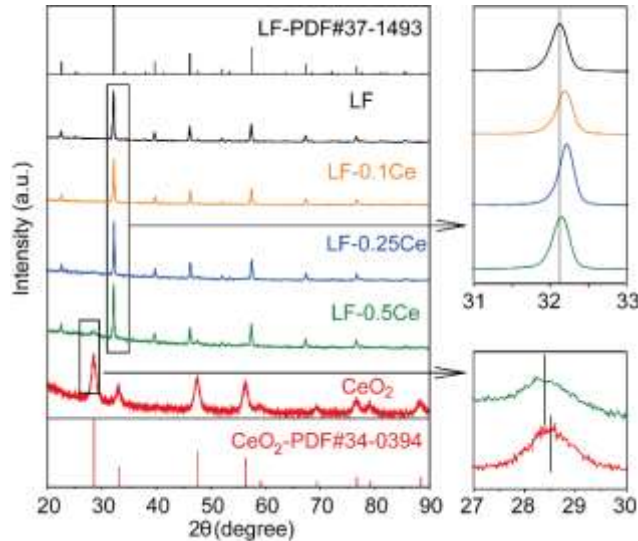
Figure 1. XRD patterns of LF, LF-0.1Ce, LF-0.25Ce, LF-0.5Ce, and CeO$_2$ powders, and the zoom-in image within the region from 31° to 33° and the region from 27° to 30°.

The TEM images of LF (Figure 2a, 2b) show the particle size of tens to several hundred nanometers and the high crystallinity. The TEM images of LF-0.25Ce (Figure 2c, 2d) show uniform deposition of ~5 nm CeO$_2$ nanoparticles on LF. The characteristic d-spacing of LF (111) (0.350 nm) and CeO$_2$ (111) (0.312 nm) are close to each other, which assists the formation of a compact heterojunction structure with ideal interface.[29] Figure 2e displays the high-angle annular dark-field scanning transmission electron microscopy (HAADF-STEM) image of the LF-0.25Ce sample at an interface region, where the outer nanoparticles and the inner bulk regions can be clearly distinguished. EDX and EELS spectra was then collected for the elemental composition analysis. In the EDX spectrum (Figure S4)**,** the energy positions of La, Fe, and Ce were too close which impedes the identification and quantification of the three elements. In contrast, the EELS spectra (Figure 2f) show a high resolution of the energy position of the three elements, with certain distinction between Fe L-edge (centered at 710 and 722 eV), La M-edge (centered at 834 and 851 eV), and Ce M-edge (centered at 882 and 900 eV). Therefore, we extracted the EELS spectra (Figure 2f) at region A, B, C, and D labeled in Figure 2e to scrutinize the spatial-resolved elemental composition**.** Region A shows intense signal of Fe L-edge and La M-edge with the atomic ratio close to 1, which is consistent with the dominant composition of LF phase at the bulk region. In comparison, the outer B, C, and D regions

show strong intensity of Ce M-edge corresponding to the dominant composition of CeO_2 nanoparticles. Interestingly, the outer regions also present weak La M-edge signals but no obvious Fe signals, indicating the selective La diffusion from the parent LF to the CeO_2 phase, which validates the strong interaction between the two phases. The EELS-mapping images (Figure 2g) clearly displays the different distribution of La, Fe, and Ce at the hybrid interface. Fe is confined at the inner region, Ce is confined at the outer region, whereas La distributes in both inner and outer regions, which further confirms the selective interfacial La diffusion. Moreover, due to the larger ionic radius of La^{3+} (1.16 Å) than that of Ce^{4+} (0.97 Å) with octahedral coordination,[28] the La incorporation in CeO_2 phase can lead to the lattice expansion, which is in accordance with the XRD peak shift of CeO_2 (111) to the lower angle as observed in Figure 1.
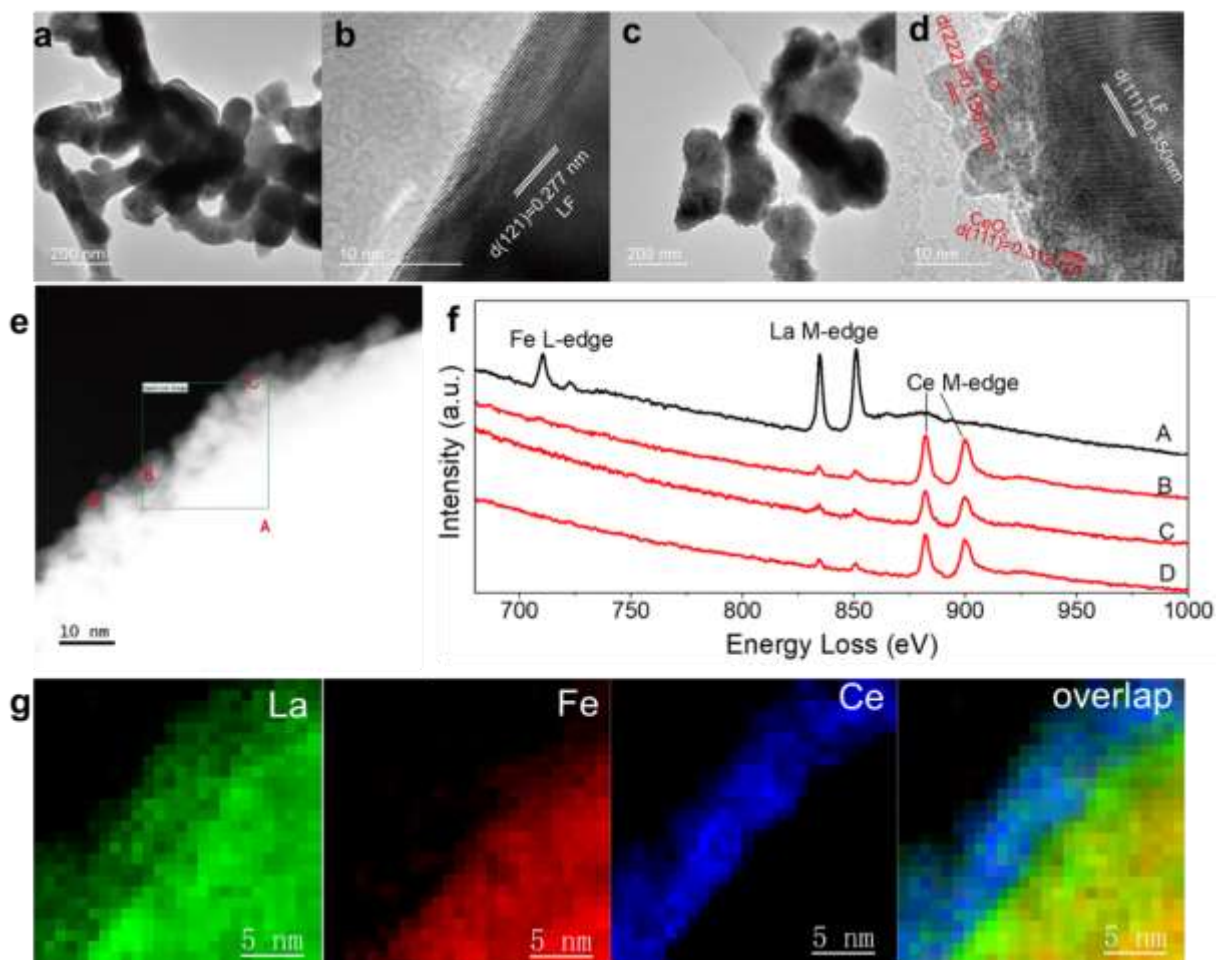
Figure 2. TEM and HRTEM images of (a, b) LF and (c, d) LF-0.25Ce. (e) HAADF-STEM image of LF-0.25Ce. (f) EELS spectra of the inner (point A) and ourter (point B, C, and D) regions labelled in (e). (g) STEM-EELS elemental mapping images of La, Fe, and Ce of the green-squared region labelled in (e).

XPS was further performed to investigate the change of surface elements induced by building the hybrid. The coexistence of Fe and Ce in the material hinders the reliable quantification of the atomic ratio due to the overlap of the binding energies between Fe 2p (from 704 to 736 eV) and Ce Auger (718.8 eV for Ce MN1, 733.3 eV for MN2), and thus we eliminate the quantitative analysis and focus on the valence states and chemical environment of surface elements. As compared to the bare LF, the LF-0.25Ce shows a higher binding energy of Fe 2p (Figure 3a), indicating the increased valance state of Fe after coating CeO_2. Simultaneously, the binding energy of Ce 3d in LF-0.25Ce shifts to lower value than that in the bare CeO_2 (Figure 3b), implying the reduced valence state of Ce induced by the interfacial interaction. The Fe 2p spectra (Figure 3c) was deconvoluted into Fe^{2+}, Fe^{3+}, and Fe^{4+} species.[30] The fitting result of the bare LF shows a few Fe^{4+} species of 9%. For LF-0.25Ce, although the exact ratio of Fe^{4+} cannot be calculated due to the interference of Ce Auger signal, we can infer an increased Fe^{4+} species in comparison to the bare LF according to the binding energy shift (Figure 3a). For the fitting result of Ce 3d (Figure 3d), the deconvoluted v_1 and u_1 peaks are assigned to Ce^{3+}, while the v_2, v_3, v_4, u_2, u_3, and u_4 peaks are assigned to Ce^{4+}.[20,31] The surface Ce^{3+} species in LF-0.25Ce (23%) were increased as compared to that in the bare CeO_2 (18%). The O 1s spectra (Figure 3e) were deconvoluted into the adsorbed O species (O_{abs}), lattice oxygen (O_L), and oxygen vacancies (O_V).[14] The bare LF shows no apparent O_V. The bare CeO_2 has intrinsic O_V (6%) that coincides with its abundant Ce^{3+} species, which also agrees with the characteristic O_V signal observed in the Raman spectrum (Figure S1).[32] Furthermore, the hybrid LF-0.25Ce shows higher intensity of O_V (16%) than the single component LF and CeO_2.
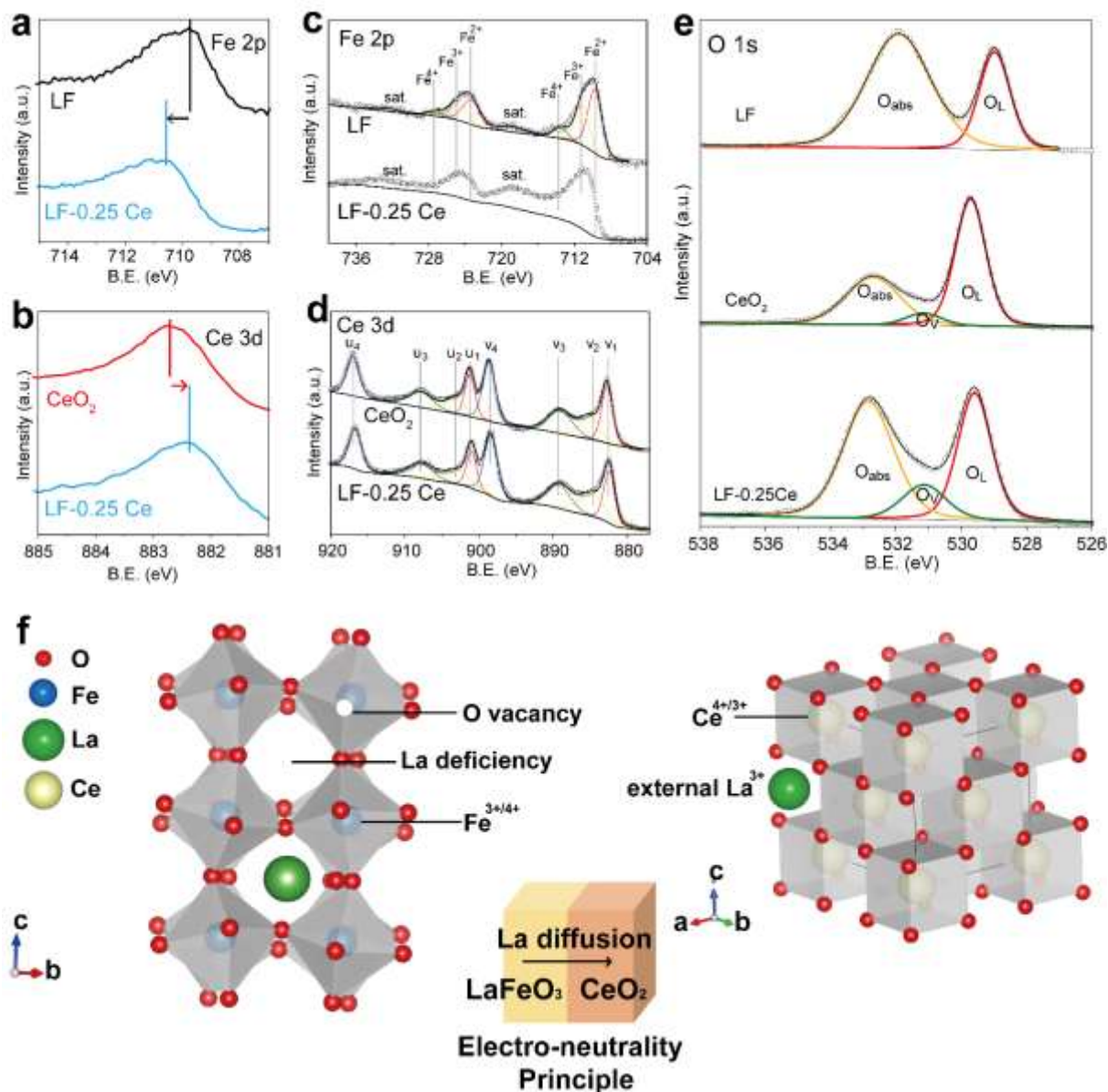
Figure 3. XPS spectra of LF, LF-0.25Ce, and CeO_2. The binding energy shift of (a) Fe and (b) Ce in the hybrid as compared to that in the single components. The peak fitting result of (c) Fe 2p, (d) Ce 3d, and (e) O 1s. (f) Schematic illustration for the hybrid-induced change of chemical enviroment of the interface elements according to the electro-neutrality principle.

The above XPS analysis proves that building hybrids induces significant changes of the chemical environment of surface elements. The changes could be attributed to the previously verified selective interfacial La diffusion according to the electro-neutrality principle.[5,33] As illustrated in Figure 3f, the incorporation of foreign La cations into the CeO_2 phase brings excessive positive charges, which stimulates the reduction of Ce valence state for charge compensation. Simultaneously, the loss of La cations in LF lattice leads to the decrease of positive charges, thus promoting the increase of Fe valence

10

state and the formation of O vacancies for electro-neutrality. Consistently, the strategy of creating A-site deficiency in perovskite oxides has also been reported by previous studies, where abundant Fe^{4+} or other high-valent B-site species as well as oxygen vacancies were realized towards higher oxygen electrolysis activity.[26,34] Moreover, according to previous reports, high valent transition metal species are regarded as the driving component for the activation of OER catalytic mechanism, and O_V sites always assist the adsorption of oxygen intermediate species during OER.[35,36] Therefore, the hybrid-induced high valent Fe^{4+} species and abundant oxygen vacancies are beneficial features for OER electrocatalysis.

To testify the influence of the hybrid effect on the OER activity, electrochemical tests were carried out. As shown in the LSV curves in 0.1 M KOH (Figure 4a) and 1 M KOH (Figure 4b), LF-0.1Ce and LF-0.25Ce exhibit enhanced OER activity as compared to the bare LF, which verifies the advantage of hybrid catalysts. With the further increase of CeO_2 loading, the LF-0.5Ce sample shows decreased OER activity, which is due to the large ratio of the catalytically inert CeO_2 component. It should be worthy to optimize the spatial configuration of the hybrid in the future work, and thus to increase the exposure of the catalytic component and maximize the beneficial effect of interface engineering towards a further activity improvement. To validate that the activity enhancement results from the hybrid effect instead of the solution treatment during the CeO_2 growth, a control experiment was carried out, and the LF-control with the absence of Ce shows no activity improvement as compared to the pristine LF (Figure S5). The potentials at 10 mA cm^{-2} of LF-0.25Ce and LF-0.1Ce (~1.65 V_{RHE} in 0.1 M KOH，~1.56 V_{RHE} in 1 M KOH) are about 20 mV lower than that of the bare LF (~1.67 V_{RHE} in 0.1 M KOH, ~1.58 V_{RHE} in 1 M KOH). The activity improvement is relatively small in the low current density region and grows more significant in the large current density region. The Tafel slopes were further calculated to assess the OER kinetics of the bare and hybrid electrocatalysts (Figure 4c and 4d, in 0.1 M KOH). In the low current density region (j<10 mA cm^{-2}), the LF, LF-0.1Ce, and LF-0.25Ce show very close Tafel slopes of 67.8, 67.3, 71.5 mV dec^{-1}, respectively. In comparison, in the

large current density region ($j>10$ mA cm^{-2}), the Tafel slopes of hybrid catalyst LF-0.1Ce (113.2 mV dec^{-1}) and LF-0.25Ce (118.4 mV dec^{-1}) are significantly lower than that of the bare LF (221.3 mV dec^{-1}), indicating the accelerated OER kinetics induced by CeO$_2$. The Tafel slopes in 1 M KOH also show a similar current density-dependent feature (Figure S6). This current density-dependent magnitude of activity improvement might be due to the switch of rate-determining step. According to the previous research, the large OER current density in alkaline solution would cause a quick consumption of OH$^-$ near the electrode surface, thus leading to decreased local pH that switches the OER rate-determining step.[37-39] However, the detailed mechanism in our LF-CeO$_2$ hybrid system is still not clear which requires further in-depth study.

The electrochemically effective surface area (ECSA) was estimated by the double layer capacitance (C$_{dl}$) through measuring the capacitive currents of the electrocatalyst within the non-Faradic potential region from 0 to 0.1 V vs. Hg/HgO (Figure S7a-S7d). LF, LF-0.1Ce, LF-0.25Ce, and LF-0.5Ce show C$_{dl}$ values of 0.86, 0.97, 1.11, and 0.72 mF cm^{-2} (Figure 4e), respectively, and they are converted to the ECSA value by the specific capacitance of 40 µF cm^{-2} per cm$^2_{ECSA}$.[40] The ECSA displays similar trend with the BET-specific area (Figure S7e), which can be ascribed to the change of surface roughness induced by coating CeO$_2$ (Figure S3). Figure 4f displays the mass activity and specific activity at the overpotential of 400 mV. As compared to the bare LF (8.0 A g^{-1}), LF-0.1Ce (13.1 A g^{-1}) and LF-0.25Ce (12.2 A g^{-1}) deliver higher mass activity whereas LF-0.5Ce (5.7 A g^{-1}) shows lower value. The specific activity of the electrocatalysts were calculated by normalizing the geometric current densities (η=400 mV) to their BET specific surface area, which gives the results of 0.16, 0.19, 0.18, and 0.15 mA cm$^{-2}_{oxide\text{-}BET}$ for LF, LF-0.1Ce, LF-0.25Ce, LF-0.5Ce, respectively (Figure 4e). The ECSA-normalized current densities also deliver the consistent trend of 0.18, 0.27, 0.22, and 0.16 mA cm$^{-2}_{oxide\text{-}ECSA}$ for LF, LF-0.1Ce, LF-0.25Ce, and LF-0.5Ce, respectively (Figure 4f). In a word, LF-0.1Ce and LF-0.25Ce shows increased specific activity than the bare LF, which demonstrates that the intrinsic OER activity of the hybrid electrocatalyst can be improved by the

increased oxygen vacancies and high-valent Fe species.

Furthermore, the long-term durability of the electrocatalysts were evaluated by performing the chronopotentiometry test at 5 mA cm^{-2} (Figure 4g). After 10 h test, the bare LF shows an overpotential increasement of 0.11 V whereas LF-0.25Ce shows a relatively more stable curve with overpotential increasement of 0.06V, indicating that the OER stability of the electrocatalyst was also improved by building the LF-CeO$_2$ hybrid. The samples after chronopotentiometry test (LF-aft and LF-0.25Ce-aft) still preserve the original LaFeO$_3$ perovskite structure and the as indicated by the XRD patterns (Figure S8). Besides, the TEM images of LF-aft (Figure S9a) and LF-0.25Ce-aft (Figure S9b) shows that original morphology, and the well-attached interface between LF and CeO$_2$ were also retained. The HRTEM image of LF-aft (Figure 4h) shows clear lattice of LF in the bulk region and an amorphous surface layer evolved from the long-term OER condition, suggesting the lattice-oxygen-participated mechanism (LOM) of OER on LF.[41,42] For the HRTEM image of LF-0.25Ce-aft (Figure 4i, Figure S9c and S9d), the lattice string of CeO$_2$ can be clearly identified whereas the LF lattice is difficult to identify. The result indicates that LF-0.25Ce-aft has a higher degree of surface amorphization than LF-aft, which is also consistent with the increased oxygen vacancy of LF-0.25Ce compared to that of the bare LF as verified before (Figure 3e). Accordingly, we infer that the CeO$_2$ decoration can activate the lattice oxygen of LF and thus enhance the LOM process towards a higher OER activity. Some other recent studies on perovskite oxide-based electrocatalysts also reported the similar mechanism as we observed here, namely activating the LOM process of metal oxides for OER activity promotion by building hybrids or increasing the concentration of oxygen vacnacy.[41,43]
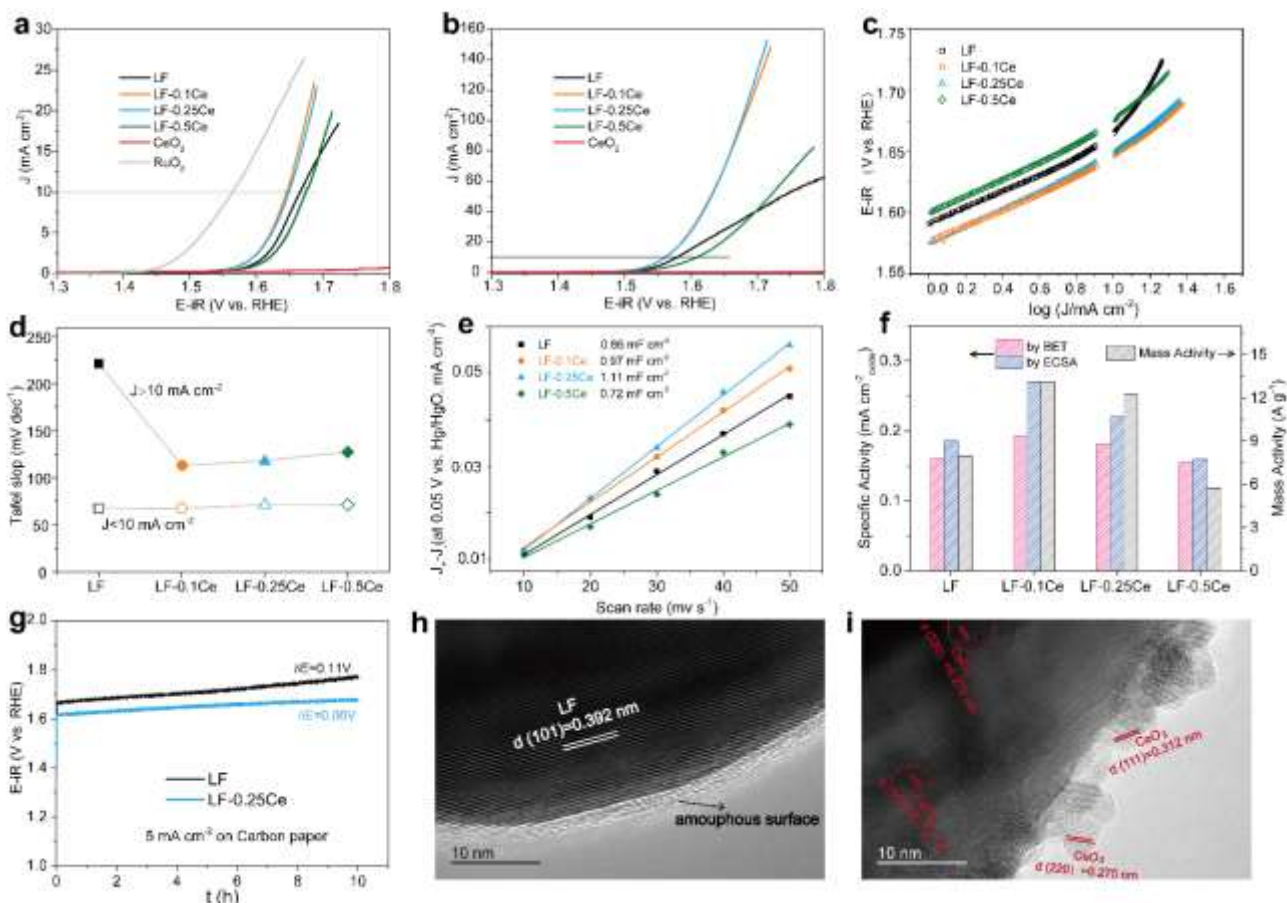
Figure 4. LSV curves of LF, LF-0.1Ce, LF-0.25Ce, LF-0.5Ce, CeO_2, and RuO_2 in (a) 0.1 M KOH and (b) 1M KOH electrolyte. (c) Tafel plots and (d) the corresponding Tafel slope values of LF, LF-0.1Ce, LF-0.25Ce, and LF-0.5Ce in 0.1 M KOH electrolyte. (e) Plots of capacitive current densities versus scan rates for the calculaiton of double layer cpacitance. (f) Mass activity and specific activity of of LF, LF-0.1Ce, LF-0.25Ce, and LF-0.5Ce in 0.1 M KOH electrolyte. (g) Chronopotentiometry test of LF and LF-0.25Ce in 0.1 M KOH electrolyte. HRTEM images of (h) LF-aft and (i) LF-0.25Ce-aft.

Figure 5 shows the EIS spectra of the bare and hybrid samples. In the Nyquist plots (Figure 5a), the real axis diameter of the semicircle is an indicator of the catalyst-electrolyte interfacial charge transfer resistance. The hybrids exhibit increased interfacial charge transfer resistances as compared to the bare LF, and the resistances grow larger with the increasing Ce loading amount. This can be attributed to the poor electronic conductivity of CeO_2.[44] Increasing the conductivity of CeO_2 by some heteroatom doping might further improve the OER activity of the hybrid. In the Bode plots (Figure 5b), the peak frequency value reflects the time scale of the catalyst-electrolyte interfacial charge transfer.[45,46] The hybrids LF-0.1Ce and LF-0.25Ce show higher peak frequencies than the bare LF,

14

which is consistent with the OER activity variation trend, further confirming the improved OER kinetics induced by the hybrid effect.
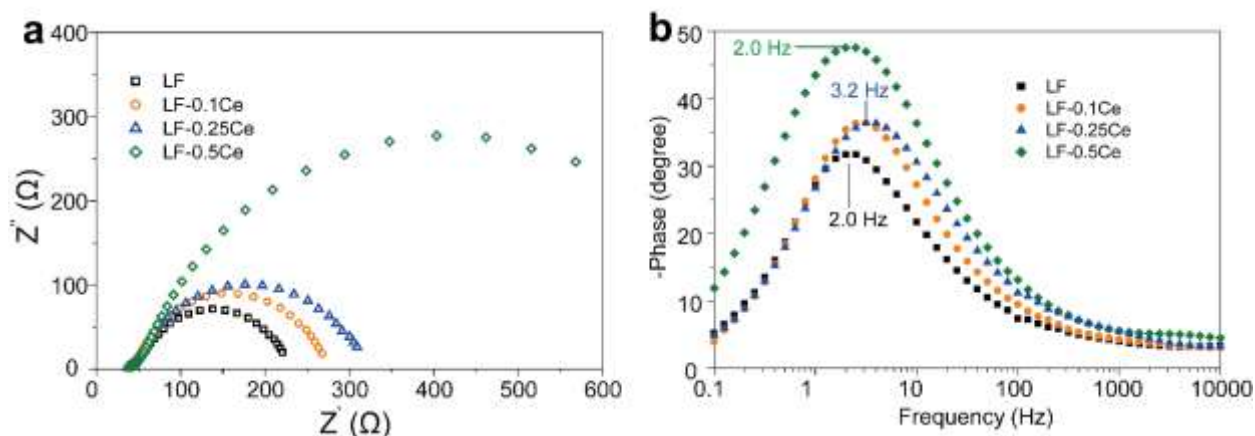

Figure 5. Electrochemical impedance spectra of LF, LF-0.1Ce, LF-0.25Ce, and LF-0.5Ce at 0.7 V vs. Hg/HgO in 0.1 M KOH displayed as (a) Nyquist plots and (b) Bode plots.

Conclusions

In summary, we synthesized the hybrid electrocatalyst of LaFeO$_3$/CeO$_2$ and demonstrated an OER activity enhancement induced by the hybrid effect. A selective interfacial La diffusion from LaFeO$_3$ to CeO$_2$ occurs in the hybrid as evidenced by the ELLS spectra and elemental mapping. Moreover, the loss of La cations in LF lattice promotes the formation of high valent Fe species and oxygen vacancies according to the electro-neutrality principle, which further facilitate the OER electrocatalysis. This work proves that the interfacial elemental redistribution plays a critical role in tuning the chemical environment of the interface elements, which might provide guidance for the design and mechanism study of other hybrid electrocatalyst systems.

Acknowledgements

Supporting Information description

Raman spectra; N_2 adsorption-desorption curves; SEM images; EDX spectrum; LSV curves of LF-control; the Tafel slopes tested in 1 M KOH; cyclic voltammetry curves for ECSA measurement; XRD patterns and TEM images of samples after the durability test

Conflict of interests

The authors declare no conflict of interests.

References

（1） Hunter, B. M.; Gray, H. B.; Muller, A. M., Earth-Abundant Heterogeneous Water Oxidation Catalysts. *Chem. Rev.* **2016,** *116* (22), 14120-14136.

（2） Jiao, Y.; Zheng, Y.; Jaroniec, M.; Qiao, S. Z., Design of electrocatalysts for oxygen- and hydrogen-involving energy conversion reactions. *Chem. Soc. Rev.* **2015,** *44* (8), 2060-86.

（3） Tahir, M.; Pan, L.; Idrees, F.; Zhang, X. W.; Wang, L.; Zou, J. J.; Wang, Z. L., Electrocatalytic oxygen evolution reaction for energy conversion and storage: A comprehensive review. *Nano Energy* **2017,** *37*, 136-157.

（4） Song, J.; Wei, C.; Huang, Z. F.; Liu, C.; Zeng, L.; Wang, X.; Xu, Z. J., A review on fundamentals for designing oxygen evolution electrocatalysts. *Chem. Soc. Rev.* **2020,** *49* (7), 2196-2214.

（5） Dai, Y.; Yu, J.; Cheng, C.; Tan, P.; Ni, M., Mini-review of perovskite oxides as oxygen electrocatalysts for rechargeable zinc–air batteries. *Chem. Eng. J.* **2020,** *397*, 125516.

（6） Long, X.; Lin, H.; Zhou, D.; An, Y.; Yang, S., Enhancing Full Water-Splitting Performance of Transition Metal Bifunctional Electrocatalysts in Alkaline Solutions by Tailoring CeO_2–Transition Metal Oxides–Ni Nanointerfaces. *ACS Energy Lett.* **2018,** *3* (2), 290-296.

（7） Chen, J.; Fan, C.; Hu, X.; Wang, C.; Huang, Z.; Fu, G.; Lee, J. M.; Tang, Y., Hierarchically Porous Co/Co_x My (M = P, N) as an Efficient Mott-Schottky Electrocatalyst for Oxygen Evolution in Rechargeable Zn-Air Batteries. *Small* **2019,** *15* (28), e1901518.

（8） Zhang, Y. Q.; Li, M.; Hua, B.; Wang, Y.; Sun, Y. F.; Luo, J. L., A strongly cooperative spinel nanohybrid as an efficient bifunctional oxygen electrocatalyst for oxygen reduction reaction and oxygen evolution reaction. *Appl. Catal., B* **2018,** *236*, 413-419.

（9） Ma, N.; Chen, G.; Zhu, Y.; Sun, H.; Dai, J.; Chu, H.; Ran, R.; Zhou, W.; Cai, R.; Shao, Z., A Self-Assembled Hetero-Structured Inverse-Spinel and Anti-Perovskite Nanocomposite for Ultrafast Water Oxidation. *Small* **2020,** *16* (31), e2002089.

（10） Gui, L.; Wang, Z.; Zhang, K.; He, B.; Liu, Y.; Zhou, W.; Xu, J.; Wang, Q.; Zhao, L., Oxygen vacancies-rich $Ce_{0.9}Gd_{0.1}O_{2-\delta}$ decorated $Pr_{0.5}Ba_{0.5}CoO_{3-\delta}$ bifunctional catalyst for efficient and long-lasting rechargeable Zn-air batteries. *Appl. Catal., B* **2020,** *266*, 118656.

（11） She, S. X.; Zhu, Y. L.; Chen, Y. B.; Lu, Q.; Zhou, W.; Shao, Z. P., Realizing Ultrafast Oxygen Evolution by Introducing Proton Acceptor into Perovskites. *Adv. Energy Mater.* **2019,** *9* (20), 1900429.

（12） Wang, X.; Sunarso, J.; Lu, Q.; Zhou, Z.; Dai, J.; Guan, D.; Zhou, W.; Shao, Z., High-Performance Platinum-Perovskite Composite Bifunctional Oxygen Electrocatalyst for Rechargeable Zn–Air Battery. *Adv. Energy Mater.* **2019,** *10* (5), 1903271.

（13） Lu, Q.; Guo, Y.; Mao, P.; Liao, K.; Zou, X.; Dai, J.; Tan, P.; Ran, R.; Zhou, W.; Ni, M.; Shao, Z., Rich atomic interfaces between sub-1 nm RuO_x clusters and porous Co_3O_4 nanosheets boost oxygen electrocatalysis bifunctionality for advanced Zn-air batteries. *Energy Stor. Mater.* **2020,** *32*, 20-29.

（14） Qiu, B. C.; Wang, C.; Zhang, N.; Cai, L. J.; Xiong, Y. J.; Chai, Y., CeO_2-Induced Interfacial Co^{2+} Octahedral Sites and Oxygen Vacancies for Water Oxidation. *ACS Catal.* **2019,** *9* (7), 6484–6490.

（15） Hou, J.; Sun, Y.; Wu, Y.; Cao, S.; Sun, L., Promoting Active Sites in Core-Shell Nanowire Array as Mott-Schottky Electrocatalysts for Efficient and Stable Overall Water Splitting. *Adv. Funct. Mater.* **2018,** *28* (4), 1704447.

（16） Sun, Z.; Wang, Y.; Zhang, L.; Wu, H.; Jin, Y.; Li, Y.; Shi, Y.; Zhu, T.; Mao, H.; Liu, J.; Xiao, C.; Ding, S., Simultaneously Realizing Rapid Electron Transfer and Mass Transport in Jellyfish-Like Mott–Schottky Nanoreactors for Oxygen Reduction Reaction. *Adv. Funct. Mater.* **2020,** *30* (15), 1910482.

（17） Wang, X. R.; Liu, J. Y.; Liu, Z. W.; Wang, W. C.; Luo, J.; Han, X. P.; Du, X. W.; Qiao, S. Z.; Yang, J., Identifying the Key Role of Pyridinic-N-Co Bonding in Synergistic Electrocatalysis for Reversible ORR/OER. *Adv. Mater.* **2018,** *30* (23), 1800005.

（18） Ji, X.; Wang, K.; Zhang, Y.; Sun, H.; Zhang, Y.; Ma, T.; Ma, Z.; Hu, P.; Qiu, Y. J. S. E., MoC based Mott–Schottky electrocatalyst for boosting the hydrogen evolution reaction performance. *Sustain. Energy Fuels* **2020,** *4* (1), 407-416.

（19） Gao, W.; Xia, Z.; Cao, F.; Ho, J. C.; Jiang, Z.; Qu, Y., Comprehensive Understanding of the Spatial Configurations of CeO_2
 in NiO for the Electrocatalytic Oxygen Evolution Reaction: Embedded or Surface-Loaded. *Adv. Funct. Mater.* **2018,** *28* (11), 1706056.

（20） Liu, Y.; Ma, C.; Zhang, Q. H.; Wang, W.; Pan, P. F.; Gu, L.; Xu, D. D.; Bao, J. C.; Dai, Z. H., 2D Electron Gas and Oxygen Vacancy Induced High Oxygen Evolution Performances for Advanced Co_3O_4/CeO_2 Nanohybrids. *Adv. Mater.* **2019,** *31* (21), 1900062.

（21） Seong, A.; Kim, J.; Kwon, O.; Jeong, H. Y.; Gorte, R. J.; Vohs, J. M.; Kim, G., Self-reconstructed interlayer derived by in-situ Mn diffusion from $La_{0.5}Sr_{0.5}MnO_3$ via atomic layer deposition for an efficient bi-functional electrocatalyst. *Nano Energy* **2020,** *71*, 104564.

（22） Feng, J. X.; Ye, S. H.; Xu, H.; Tong, Y. X.; Li, G. R., Design and Synthesis of FeOOH/CeO_2 Heterolayered Nanotube Electrocatalysts for the Oxygen Evolution Reaction. *Adv.*

Mater. **2016,** *28* (23), 4698-703.

（23） Zhang, H. Y.; Du, J. G.; Niu, D. F.; Hu, S. Z.; Zhang, X. S., Synthesis and Characterization of Fe^{3+} and CeO_2 Co-decorated NiOOH Electrocatalysts Supported by Nickel Foam for the Oxygen Evolution Reaction. *Int. J. Electrochem.Sci.* **2019,** *14* (7), 6532-6545.

（24） Haxel, G., *Rare earth elements: critical resources for high technology*. US Department of the Interior, US Geological Survey: 2002; Vol. 87.

（25） Liu, Z. Q.; Li, N.; Zhao, H. Y.; Zhang, Y.; Huang, Y. H.; Yin, Z. Y.; Du, Y. P., Regulating the active species of $Ni(OH)_2$ using CeO_2: 3D $CeO_2/Ni(OH)_2$/carbon foam as an efficient electrode for the oxygen evolution reaction. *Chem. Sci.* **2017,** *8* (4), 3211-3217.

（26） Zhu, Y. L.; Zhou, W.; Yu, J.; Chen, Y. B.; Liu, M. L.; Shao, Z. P., Enhancing Electrocatalytic Activity of Perovskite Oxides by Tuning Cation Deficiency for Oxygen Reduction and Evolution Reactions. *Chem. Mater.* **2016,** *28* (6), 1691-1697.

（27） Zhu, Y.; Sunarso, J.; Zhou, W.; Jiang, S.; Shao, Z., High-performance $SrNb_{0.1}Co_{0.9-x}Fe_xO_{3-\delta}$perovskite cathodes for low-temperature solid oxide fuel cells. *J. Mater. Chem. A* **2014,** *2* (37), 15454-15462.

（28） Lide, D. R., *CRC Handbook of Chemistry and Physics, 90th ed., (CD-ROM Version 2010)*. CRC Press/Taylor and Francis: Boca Raton, FL, USA, 2009.

（29） Liu, T.; Gao, W.; Wang, Q.; Dou, M.; Zhang, Z.; Wang, F., Selective loading of atomic Pt on a $RuCeO_x$ support enables stable hydrogen evolution at high current densities. *Angew. Chem. Int. Ed.* **2020**.

（30） She, S.; Yu, J.; Tang, W.; Zhu, Y.; Chen, Y.; Sunarso, J.; Zhou, W.; Shao, Z., Systematic Study of Oxygen Evolution Activity and Stability on $La_{1-x}Sr_xFeO_{3-\delta}$ Perovskite Electrocatalysts in Alkaline Media. *ACS Appl. Mater. Interfaces* **2018,** *10* (14), 11715-11721.

（31） He, X.; Yi, X.; Yin, F.; Chen, B.; Li, G.; Yin, H., Less active CeO_2 regulating bifunctional oxygen electrocatalytic activity of Co_3O_4@ N-doped carbon for Zn–air batteries. *J. Mater. Chem. A* **2019,** *7* (12), 6753-6765.

（32） Liang, F. L.; Yu, Y.; Zhou, W.; Xu, X. Y.; Zhu, Z. H., Highly defective CeO_2 as a promoter for efficient and stable water oxidation. *J. Mater. Chem. A* **2015,** *3* (2), 634-640.

（33） Niu, B.; Jin, F.; Feng, T.; Zhang, L.; Zhang, Y.; He, T., A-site deficient $(La_{0.6}Sr_{0.4})_{1-x}Co_{0.2}Fe_{0.6}Nb_{0.2}O_{3-\delta}$ symmetrical electrode materials for solid oxide fuel cells. *Electrochim. Acta* **2018,** *270*, 174-182.

（34） Yuan, R.-h.; He, Y.; He, W.; Ni, M.; Leung, M. K., Bifunctional electrocatalytic activity of $La_{0.8}Sr_{0.2}MnO_3$-based perovskite with the A-site deficiency for oxygen reduction and evolution reactions in alkaline media. *Applied Energy* **2019,** *251*, 113406.

（35） Feng, C.; Faheem, M. B.; Fu, J.; Xiao, Y. Q.; Li, C. L.; Li, Y. B., Fe-Based Electrocatalysts for Oxygen Evolution Reaction: Progress and Perspectives. *ACS Catal.* **2020,** *10* (7), 4019-4047.

（36） Xu, W.; Apodaca, N.; Wang, H.; Yan, L.; Chen, G.; Zhou, M.; Ding, D.; Choudhury,

P.; Luo, H., A-site Excessive $(La_{0.8}Sr_{0.2})_{1+x}MnO_3$ Perovskite Oxides for Bifunctional Oxygen Catalyst in Alkaline Media. *ACS Catal.* **2019,** *9* (6), 5074-5083.

（37） Fang, Y.-H.; Liu, Z.-P. J. A. C., Tafel kinetics of electrocatalytic reactions: from experiment to first-principles. *ACS Catal.* **2014,** *4* (12), 4364-4376.

（38） Zhang, Y.; Zhang, H.; Liu, A.; Chen, C.; Song, W.; Zhao, J., Rate-limiting O–O bond formation pathways for water oxidation on hematite photoanode. *J. Am. Chem. Soc.* **2018,** *140* (9), 3264-3269.

（39） Sun, S.; Sun, Y.; Zhou, Y.; Shen, J.; Mandler, D.; Neumann, R.; Xu, Z. J., Switch of the Rate-Determining Step of Water Oxidation by Spin-Selected Electron Transfer in Spinel Oxides. *Chem. Mater.* **2019,** *31* (19), 8106-8111.

（40） Zhang, R.; Wang, X.; Yu, S.; Wen, T.; Zhu, X.; Yang, F.; Sun, X.; Wang, X.; Hu, W., Ternary $NiCo_2P_x$ nanowires as pH-universal electrocatalysts for highly efficient hydrogen evolution reaction. *Adv. Mater.* **2017,** *29* (9), 1605502.

（41） Pan, Y.; Xu, X.; Zhong, Y.; Ge, L.; Chen, Y.; Veder, J.-P. M.; Guan, D.; O'Hayre, R.; Li, M.; Wang, G., Direct evidence of boosted oxygen evolution over perovskite by enhanced lattice oxygen participation. *Nat. Commun.* **2020,** *11* (1), 1-10.

（42） Grimaud, A.; Diaz-Morales, O.; Han, B.; Hong, W. T.; Lee, Y.-L.; Giordano, L.; Stoerzinger, K. A.; Koper, M. T.; Shao-Horn, Y., Activating lattice oxygen redox reactions in metal oxides to catalyse oxygen evolution. *Nat. Chem.* **2017,** *9* (5), 457-465.

（43） Wang, X.; Pan, Z.; Chu, X.; Huang, K.; Cong, Y.; Cao, R.; Sarangi, R.; Li, L.; Li, G.; Feng, S., Atomic-scale insights into surface lattice oxygen activation at the spinel/perovskite interface of $Co_3O_4/La_{0.3}Sr_{0.7}CoO_3$. *Angew. Chem.* **2019,** *131* (34), 11846-11851.

（44） Li, M.; Wang, Y.; Zheng, Y.; Fu, G.; Sun, D.; Li, Y.; Tang, Y.; Ma, T., Gadolinium-Induced Valence Structure Engineering for Enhanced Oxygen Electrocatalysis. *Adv. Energy Mater.* **2020,** *10* (10), 1903833.

（45） Malara, F.; Minguzzi, A.; Marelli, M.; Morandi, S.; Psaro, R.; Dal Santo, V.; Naldoni, A., α-Fe_2O_3/NiOOH: an effective heterostructure for photoelectrochemical water oxidation. *ACS Catal.* **2015,** *5* (9), 5292-5300.

（46） Malara, F.; Fabbri, F.; Marelli, M.; Naldoni, A., Controlling the surface energetics and kinetics of hematite photoanodes through few atomic layers of NiO_x. *ACS Catal.* **2016,** *6* (6), 3619-3628.

Abstract graphic